

Energy-based analysis and anisotropic spectral distribution of internal gravity waves in strongly stratified turbulence

Naoto Yokoyama*

Department of Mechanical Science and Bioengineering, Osaka University, Toyonaka 560-8531, Japan

Masanori Takaoka†

Department of Mechanical Engineering, Doshisha University, Kyotanabe 610-0394, Japan

(Dated: September 20, 2019)

Stratified turbulence shows scale- and direction-dependent anisotropy and the coexistence of weak turbulence of internal gravity waves and strong turbulence of eddies. Straightforward application of standard analyses developed in isotropic turbulence sometimes masks important aspects of the anisotropic turbulence. To capture detailed structures of the energy distribution in the wave-number space, it is indispensable to examine the energy distribution with non-integrated spectra by fixing the codimensional wave-number component or in the two-dimensional domain spanned by both the horizontal and vertical wave numbers. Indices which separate the range of the anisotropic weak-wave turbulence in the wave-number space are proposed based on the decomposed energies. In addition, the dominance of the waves in the range is also verified by the small frequency deviation from the linear dispersion relation. In the wave-dominant range, the linear wave periods given by the linear dispersion relation are smaller than approximately one third of the eddy-turnover time. The linear wave periods reflect the anisotropy of the system, while the isotropic Brunt-Väisälä period is used to evaluate the Ozmidov wave number, which is necessarily isotropic. It is found that the time scales in consideration of the anisotropy of the flow field must be appropriately selected to obtain the critical wave number separating the weak-wave turbulence.

I. INTRODUCTION

Turbulence in nature essentially has anisotropy especially in large scales. Theoretical approaches in turbulence researches originate from Kolmogorov's local isotropy hypothesis, and have been extended to researches in anisotropic turbulence systems. Numerical simulations of high Reynolds-number turbulent flows and their analyses are developed also in homogeneous statistically-isotropic turbulence systems, and are often incorporated in anisotropic turbulence systems simply. It is essential to introduce appropriate analytical tools which do not diminish scale- and direction-dependent anisotropic properties in the anisotropic turbulence.

Stratified turbulence is one of the most fundamental turbulence systems which have statistical anisotropy, and is observed in the oceans and the atmosphere. The gravity produces the density or thermal stratification, and makes statistical differences in energy distribution between the vertical direction and the horizontal direction. The breaking of the internal gravity waves affects the global climate and our lives; the upwelling due to breaking is an important part of the thermohaline circulation in the oceans [1], and the breaking in the atmosphere sometimes causes clear-air turbulence that may expose aircraft flight to risk [2]. The breaking corresponds the energy transfer from waves to vortices.

Various kinds of energy spectra have been reported in observations, experiments, and simulations of stratified turbulence. The variety is derived from the physical mechanisms, the length scales, and other parameters. Such different energy spectra can coexist, and the coexistence is obtained in atmospheric observations and numerical simulations [3–5]. For example, a kinetic-energy spectrum observed in atmospheric flows has a power law $K_{\perp}(k_{\perp}) \propto k_{\perp}^{-3}$ at large scales [3]. Here, k_{\perp} is a horizontal wave number, and $K_{\perp}(k_{\perp})$ is the horizontal kinetic-energy spectrum as a function of k_{\perp} . Another power law $K_{\perp}(k_{\perp}) \propto k_{\perp}^{-5/3}$ is also observed at mesoscales, and the same power law is obtained analytically and numerically [5]. Observation and theoretical prediction also have a variety of the kinetic-energy spectrum as a function of the vertical wave number k_{\parallel} : the breaking of the internal gravity waves makes the total kinetic-energy spectrum $K(k_{\parallel}) \propto k_{\parallel}^{-3}$ [6] for example. The Bolgiano-Obukhov phenomenology predicts coexistence of two power-laws in kinetic spectra: $K(k) \propto k^{-11/5}$ for $k < k_B$ and $K(k) \propto k^{-5/3}$ for $k > k_B$, where k_B is the Bolgiano wave number [7, 8]. The pioneering work for the two-dimensional energy spectrum of the internal gravity waves observed in the ocean is the Garrett-Munk spectrum, which has $K(k_{\perp}, k_{\parallel}) \propto k_{\perp}^{-2} k_{\parallel}^{-1}$ at relatively

* yokoyama@me.es.osaka-u.ac.jp

† mtakaoka@mail.doshisha.ac.jp

large wave numbers [9]. The weak turbulence theory predicts a variety of power laws including the Garrett-Munk spectrum [10]. A spectral model that allows even variability was proposed [11]. In this way, the kinetic-energy spectra as well as the potential-energy spectra are diverse, and the diversity may result from the boundary conditions and the magnitude relation between the horizontal wave number and the vertical wave number. On the other hand, when the stratification is relatively weak, the vortices are dominant in the flow, and the three-dimensional isotropic Kolmogorov turbulence appears. Then, the energy spectrum shows the Kolmogorov's power law $K(k) \propto k^{-5/3}$.

To elucidate the variability of the energy spectra at the small wave numbers and to consistently observe them, the dominant physical mechanism at a wave number is required to be evaluated. In this case, the one-dimensionalized energy spectra such as $K_{\perp}(k_{\perp})$ obtained by integration over k_{\parallel} cannot properly reflect the energy distribution in the anisotropic turbulence. The wave-number range where one of the physical mechanisms framing the anisotropic turbulence is dominant should be identified in the k_{\perp} - k_{\parallel} space.

It is the general practice to focus on time scales to find a dominant mechanism in complex dynamical systems which have multiple physics [12]. In the three-dimensional isotropic Kolmogorov turbulence, for example, the eddies in the inertial subrange have the eddy-turnover time shorter than the dissipation time, while the dissipation time is shorter than the eddy-turnover time in the dissipation range. The Kolmogorov wave number, which separates the inertial subrange and the dissipation range, is defined so that the eddy-turnover time is equal to the dissipation time.

The weak turbulence theory, which has been successfully applied to the statistical description of the nonlinear energy transfers among weakly-coupled dispersive waves, assumes that the linear time scale evaluated by the linear dispersion relation is much smaller than the nonlinear time scale of energy transfers. However, the linear time scale becomes comparable with the nonlinear time scale, and the assumption of the weak nonlinearity is violated either at small or large wave numbers in most of the wave turbulence systems [13–15]. As a result, the weak-wave turbulence and the strong turbulence coexist in many wave turbulence systems such as stratified turbulence considered here, rotating turbulence [16], magnetohydrodynamic turbulence [17], elastic-wave turbulence [18] and quantum turbulence [19].

In stratified turbulence, the Brunt-Väisälä period and the eddy-turnover time have respectively been used as the linear and nonlinear time scales. The Ozmidov wave number defined as the wave number at which these two time scales are comparable has been considered as the critical wave number that separates the strongly anisotropic turbulence and the isotropic Kolmogorov turbulence [20]. In fact, the wave numbers much larger than the Ozmidov wave number, the stratification can be almost negligible, and the isotropic Kolmogorov turbulence appears. The buoyancy wave number, which is defined by the characteristic horizontal velocity and the Brunt-Väisälä frequency, gives the scale of the shear layers and the breaking of the internal gravity waves [21].

On the other hand, the weak-wave turbulence does not appear at all the wave numbers smaller than the Ozmidov wave number or the buoyancy wave number. The anisotropic quasi-two-dimensional turbulence such as the layer-wise two-dimensional turbulence [22] and the pancake turbulence [23] exists at such small wave numbers. Neither the Ozmidov wave number nor the buoyancy wave number can identify the wave-number range where statistically-anisotropic gravity-wave turbulence is dominant because of the isotropy assumed in their derivations. The anisotropy of the time scales can be introduced by using the period given by the linear dispersion relation instead of the Brunt-Väisälä period as the linear time scale [24]. The wave number at which the period given by the linear dispersion relation and the eddy-turnover time are comparable can separate the weak-wave turbulence and the isotropic or anisotropic strong turbulence in magnetohydrodynamic turbulence [17, 25–27]. However, it is not clear in rotating turbulence [28].

In this paper, direct numerical simulations of strongly stratified turbulence are performed, and anisotropic properties of internal gravity-wave turbulence are characterized by distribution and decomposition of energy. The organization of the paper is as follows. The numerical scheme of the direct numerical simulations and decomposition of the wave-number space and the flow field are shown in Sec. II, where some definitions of the energies to characterize the anisotropic weak-wave turbulence are provided. The numerical results are exhibited in Sec. III. Indices to identify the range of the anisotropic internal gravity-wave turbulence are proposed, and the range is examined in the two-dimensional domain spanned by both of the horizontal and vertical wave numbers. The last section is devoted to the summary.

TABLE I. Parameters in the numerical simulations. Re : horizontal Reynolds number, Re_b : buoyancy Reynolds number, Fr_\perp : horizontal Froude number, Fr_\parallel : vertical Froude number, k_O : Ozmidov wave number, k_b : buoyancy wave number. The root-mean square of the horizontal velocity is denoted by $u_{\perp\text{rms}}$. The horizontal and vertical integral length scales, ℓ_\perp and ℓ_\parallel , are defined by transverse velocity correlations.

number of grid points	$\gamma_{\mathbf{k}}$	Re	Re_b	Fr_\perp	Fr_\parallel	k_O	k_b
		$u_{\perp\text{rms}}\ell_\perp/\nu$	$\bar{\varepsilon}/(\nu N^2)$	$u_{\perp\text{rms}}/(N\ell_\perp)$	$u_{\perp\text{rms}}/(N\ell_\parallel)$	$\sqrt{N^3/\bar{\varepsilon}}$	$N/u_{\perp\text{rms}}$
2048 ³	0.5	7.7×10^4	2.1	9.0×10^{-3}	0.80	490	27
1024 ³	0.1	1.8×10^4	9.4×10^{-2}	4.9×10^{-3}	0.15	2300	76
1024 ³	0.2	1.1×10^4	0.24	9.4×10^{-3}	0.17	1200	57
1024 ³	0.5	2.5×10^4	0.80	9.6×10^{-3}	0.46	500	29
1024 ³	1	4.1×10^4	1.9	1.4×10^{-2}	1.6	260	15
1024 ³	2	3.7×10^4	4.7	1.9×10^{-2}	2.0	130	11
1024 ³	5	2.2×10^4	18	3.5×10^{-2}	1.0	53	8.2

II. FORMULATION

A. Numerical scheme

Incompressible flows in stably stratified background flow in the z direction is considered. Under the Boussinesq approximation, the governing equation for the velocity \mathbf{u} and buoyancy b is given as follows:

$$\frac{\partial}{\partial t}\mathbf{u} + (\mathbf{u} \cdot \nabla)\mathbf{u} = -\nabla p + b\mathbf{e}_z + \nu\nabla^2\mathbf{u} + \mathbf{f}, \quad (1a)$$

$$\nabla \cdot \mathbf{u} = 0, \quad (1b)$$

$$\frac{\partial}{\partial t}b + (\mathbf{u} \cdot \nabla)b = -N^2\mathbf{u} \cdot \mathbf{e}_z + \kappa\nabla^2b. \quad (1c)$$

The buoyancy b is given as $b = -g\theta'/\theta_0$ in atmospheric flows, for example, where g , θ' , and θ_0 are respectively the gravity acceleration, the temperature fluctuation, and the mean temperature. The Brunt-Väisälä frequency N is assumed to be constant. The external force \mathbf{f} is added to obtain the non-equilibrium statistically-steady state. The kinematic viscosity and the diffusion constant are respectively denoted by ν and κ .

In this work, direct numerical simulations of Eq. (1) are performed in a periodic box with the side 2π . The Fourier coefficients of the dependent variables appearing in Eq. (1), $\tilde{\mathbf{u}}_{\mathbf{k}}$, $\tilde{p}_{\mathbf{k}}$, and $\tilde{b}_{\mathbf{k}}$, are used, and the tildes are omitted below. The pseudo-spectral method with aliasing removal due to the phase shift is employed to evaluate the nonlinear term. The Runge-Kutta-Gill method is used for the time integration. The external force is added in the wave-number space to the wave-number mode in $k_f - 1/2 \leq |\mathbf{k}| < k_f + 1/2$, where the forced wave number k_f is set to 4. The external force is generated by the Ornstein-Uhlenbeck process [4] as follows. The colored noise $\hat{\mathbf{f}}_{\mathbf{k}} = (\hat{f}_{x\mathbf{k}}, \hat{f}_{y\mathbf{k}}, 0)$, which consists of two spatial components each having a complex value, is obtained for each wave number according to the following stochastic differential equation:

$$\begin{pmatrix} d\hat{\mathbf{f}}_{\mathbf{k}} \\ d\hat{\mathbf{g}}_{\mathbf{k}} \end{pmatrix} = dt \begin{pmatrix} -\alpha & 1 \\ 0 & -\alpha \end{pmatrix} \begin{pmatrix} \hat{\mathbf{f}}_{\mathbf{k}} \\ \hat{\mathbf{g}}_{\mathbf{k}} \end{pmatrix} + \begin{pmatrix} \mathbf{0} \\ \gamma_{\mathbf{k}}d\mathbf{W}_{\mathbf{k}} \end{pmatrix}, \quad (2)$$

where $d\mathbf{W}_{\mathbf{k}}$ represents the normal random variables with mean 0 and variance dt and has four independent components. The correlation time of $\hat{\mathbf{f}}_{\mathbf{k}}$ is $O(1/\alpha)$, and α is set to be N in this paper. Because $\langle |\hat{\mathbf{f}}_{\mathbf{k}}|^2 \rangle = \gamma_{\mathbf{k}}^2/\alpha$, $\gamma_{\mathbf{k}}$ is used to control the amplitude of the external force. Finally, the Fourier coefficient of the external force is set as $\mathbf{f}_{\mathbf{k}} = \hat{\mathbf{f}}_{\mathbf{k}} - \mathbf{k}(\mathbf{k} \cdot \hat{\mathbf{f}}_{\mathbf{k}})/k^2$ to satisfy the divergence-free condition.

The number of the grid points used is up to 2048³. The low-resolution simulations with 1024³ grid points are also used to examine the parameter dependence. The corresponding largest wave number k_{max} is approximately 970 or 480. The Brunt-Väisälä frequency is set to $N = 10$. The Prandtl number is set to be unity, i.e., $\nu = \kappa$, and ν is chosen so that $k_{\text{max}}/k_\eta \approx 1.2$. Here, $k_\eta = (\bar{\varepsilon}/\nu^3)^{1/4}$ is the Kolmogorov wave number, and $\bar{\varepsilon}$ denotes the mean dissipation rate of the kinetic energy. The coefficient $\gamma_{\mathbf{k}}$ to control the amplitude of the external force is varied in the simulations with 1024³ grids. The parameters in the numerical simulations and their definitions which follow those in Ref. [29] are summarized in Table I.

The initial condition of a simulation is a statistically steady state of the lower-resolution simulation. Therefore, the small wave-number modes are numerically integrated over a long time as $Nt = O(10^3)$. Because all the simulations relax to statistically steady states after some times depending on the amplitudes of the external force, the growth without stationarity reported in Ref. [30] was not observed in the simulations. The time averaging is performed to draw the spectra for $Nt = 100$ with every 12.5 in the high-resolution simulation. It might be short to remove the fluctuation at the small wave numbers, but the results shown in this paper are confirmed to be unchanged in the low-resolution simulations, where long-time averaging is performed.

B. Ratios of time scales to find the dominant physical mechanism

The Ozmidov wave number k_O has been considered as a wave number which separates the strongly anisotropic range and the isotropic range in the wave-number space. The Ozmidov wave number is given as a wave number at which the Brunt-Väisälä period $1/N$ and the eddy-turnover time of the three-dimensional (3D) isotropic turbulence $\tau_{\mathbf{k}} = 1/(ku) = (k^2\bar{\varepsilon})^{-1/3}$ are comparable, i.e., $k_O = \sqrt{N^3/\bar{\varepsilon}}$. It should be noted that the Ozmidov wave number is independent of the direction of the wave number vector, i.e., isotropic. The 3D isotropic Kolmogorov turbulence is expected to dominate at the wave numbers larger than k_O , but k_O does not necessarily determine the wave-number range where the weak gravity-wave turbulence is dominant because of the lack of the anisotropy. The buoyancy wave number $k_b = N/u_{\perp\text{rms}}$ is another wave number that characterizes the transition from the quasi-two-dimensional turbulence to the 3D isotropic turbulence. The buoyancy wave number is also isotropic.

Owing to the anisotropy, the spectral structures in the wave-number space should be investigated in the k_{\perp} - k_{\parallel} space. The theory of the critical balance states that the energy is transferred in the transitional wave-number range between the wave-dominant and vortex-dominant ranges [24]. In this theory, the wave period of the gravity wave given by the linear dispersion relation is employed as the linear time scale instead of the Brunt-Väisälä period. Note that the linear dispersion relation is anisotropic. Because $k_{\perp} \ll k_{\parallel}$ and hence $|\mathbf{u}_{\perp}| \gg |u_{\parallel}|$ owing to the divergence-free condition were assumed in Refs. [24, 31], the linear dispersion relation was rewritten as $\sigma_{2D\mathbf{k}} = Nk_{\perp}/k_{\parallel}$, and the eddy-turnover time of the two-dimensional (2D) turbulence $\tau_{2D\mathbf{k}} = 1/(k_{\perp}u_{\perp}) = (k_{\perp}^2\bar{\varepsilon})^{-1/3}$ was used as the nonlinear time. In the present work, since the strong turbulence is not only 2D but also 3D and $k_{\perp} \ll k_{\parallel}$ does not necessarily hold, the general linear dispersion relation $\sigma_{\mathbf{k}} = Nk_{\perp}/k$ is used to evaluate the linear time. Moreover, the eddy-turnover time of the 3D turbulence $\tau_{\mathbf{k}} = (k^2\bar{\varepsilon})^{-1/3}$ is used as the nonlinear time. Then, the nonlinearity is evaluated by $\chi_{\mathbf{k}} = 1/(\sigma_{\mathbf{k}}\tau_{\mathbf{k}})$. The ratio of the gravity-wave period to the 2D eddy-turnover time $\chi_{2D\mathbf{k}} = 1/(\sigma_{2D\mathbf{k}}\tau_{2D\mathbf{k}})$ is also introduced for reference.

C. Decomposition of turbulent flow

To examine the idea of the critical balance, it is indispensable to identify the wave-dominant range. The Craya-Herring (Cartesian) decomposition and the helical-mode decomposition are used for the identification in this paper.

In the Craya-Herring decomposition [4, 32], an orthonormal basis, $\mathbf{e}_1 = \mathbf{k} \times \mathbf{e}_z/k_{\perp}$, $\mathbf{e}_2 = \mathbf{k} \times \mathbf{e}_1/k$, and $\mathbf{e}_3 = \mathbf{k}/k$, is introduced. The two basis vectors \mathbf{e}_1 and \mathbf{e}_2 are defined only when \mathbf{k} and \mathbf{e}_z are not in parallel, that is, horizontal component of \mathbf{k} , k_{\perp} , is non-zero. The orthogonal basis decomposes the velocity as

$$\mathbf{u}_{\mathbf{k}} = \begin{cases} u_v\mathbf{e}_1 + u_w\mathbf{e}_2 & \text{for } k_{\perp} \neq 0 \\ \mathbf{u}_s & \text{for } k_{\perp} = 0 \end{cases}. \quad (3)$$

The Fourier component of the velocity is given by two components perpendicular to the wave-number vector \mathbf{k} because of the incompressibility $\mathbf{k} \cdot \mathbf{u}_{\mathbf{k}} = 0$. When the wave numbers with $k_{\perp} = 0$ are included, such decomposition is called the Cartesian decomposition.

When the viscosity and the diffusion are neglected for $k_{\perp} \neq 0$, the governing equation (1) can be linearized as

$$\frac{\partial u_{v\mathbf{k}}}{\partial t} = 0, \quad \frac{\partial u_{w\mathbf{k}}}{\partial t} = -\frac{k_{\perp}}{k}b_{\mathbf{k}}, \quad \frac{\partial b_{\mathbf{k}}}{\partial t} = N^2\frac{k_{\perp}}{k}u_{w\mathbf{k}}. \quad (4)$$

This linear inviscid non-diffusive equation indicates that $u_v = i\omega_z/k_{\perp}$ is a vortical mode that is not affected by the linear buoyancy term, and $u_w = -ku_z/k_{\perp}$ is a wave mode. Here, ω_z denotes the z component of the vorticity. The second equation and the third one in Eq. (4) give the linear dispersion relation of the gravity waves: $\sigma_{\mathbf{k}} = Nk_{\perp}/k$. The velocity for $k_{\perp} = 0$, $\mathbf{u}_{s\mathbf{k}_z} = \mathbf{u}_{\perp}$, represents a vertically-sheared horizontal flow. Namely, the Cartesian decomposition simply represents the decomposition of the velocity into the vortices, the waves and the shear flows at the lowest order. The Cartesian decomposition is equivalent to the normal-mode decomposition [33].

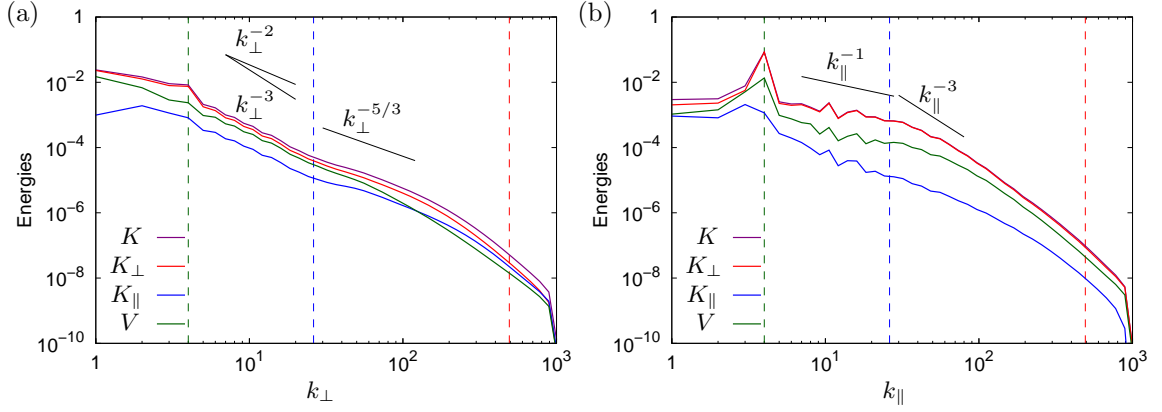


FIG. 1. Integrated energy spectra: total kinetic energy, horizontal kinetic energy, vertical kinetic energy, and potential energy. (a) as functions of horizontal wave numbers integrated over the vertical wave numbers, and (b) as functions of vertical wave numbers integrated over the horizontal wave numbers. The green, blue and red vertical dashed lines respectively show the forced wave number k_f , the buoyancy wave number k_b , and the Ozmidov wave number k_O .

The helical-mode decomposition has also been used for the decomposition of the velocity. In the helical-mode decomposition, the basis $\mathbf{h}_{\pm} = (\mathbf{e}_2 \mp i\mathbf{e}_1)/\sqrt{2}$ is the eigen vector for the curl operation, $i\mathbf{k} \times \mathbf{h}_{\pm} = \pm k\mathbf{h}_{\pm}$. Then, the velocity is decomposed as $\mathbf{u} = \xi_+\mathbf{h}_+ + \xi_-\mathbf{h}_-$, where $\xi_{\pm} = \mathbf{u} \cdot \mathbf{h}_{\mp}$ is the helical-mode intensity. Note that $\mathbf{h}_{\pm} \cdot \mathbf{h}_{\pm} = 0$ and $\mathbf{h}_{\pm} \cdot \mathbf{h}_{\mp} = 1$.

A wave-number mode \mathbf{k} has a total energy $E_{\mathbf{k}}$, which is sum of the kinetic energy $K_{\mathbf{k}} = \langle |\mathbf{u}_{\mathbf{k}}|^2 \rangle / 2$ and potential energy $V_{\mathbf{k}} = \langle |b_{\mathbf{k}}|^2 \rangle / (2N^2)$. The kinetic energy can be given by horizontal kinetic energy $K_{\perp\mathbf{k}} = K_{x\mathbf{k}} + K_{y\mathbf{k}} = (\langle |u_{x\mathbf{k}}|^2 \rangle + \langle |u_{y\mathbf{k}}|^2 \rangle) / 2$ and vertical kinetic energy $K_{\parallel\mathbf{k}} = K_{z\mathbf{k}} = \langle |u_{z\mathbf{k}}|^2 \rangle / 2$, focused on the direction of the velocity. Similarly, the Cartesian decomposition defines vortical kinetic energy $K_{v\mathbf{k}} = \langle |u_{v\mathbf{k}}|^2 \rangle / 2 = \langle |\omega_{z\mathbf{k}}|^2 \rangle / (2k_{\perp}^2)$, wave kinetic energy $K_{w\mathbf{k}} = \langle |u_{w\mathbf{k}}|^2 \rangle / 2 = k^2 \langle |u_{z\mathbf{k}}|^2 \rangle / (2k_{\perp}^2)$, and shear kinetic energy $K_{sk_z} = \langle |u_{sk_z}|^2 \rangle / 2 = \langle |u_{\perp k_z}|^2 \rangle / 2$. Because the shear flow is defined only for $k_{\perp} = 0$, it depends only on k_z . Moreover, according to the helical-mode decomposition, the kinetic energy in the m direction, where $m = x, y, z$, can be written as

$$K_{m\mathbf{k}} = \frac{K(k)}{8\pi k^2} \left(1 - \frac{k_m^2}{k^2}\right) + \frac{1}{2} \left(K_{\mathbf{k}} - \frac{K(k)}{4\pi k^2}\right) \left(1 - \frac{k_m^2}{k^2}\right) + \text{Re}[Z_{\mathbf{k}} h_{+m\mathbf{k}}^2]. \quad (5)$$

Here, $K(k)$ is the one-dimensionalized energy spectrum, and $Z_{\mathbf{k}} = \langle \xi_{+\mathbf{k}} \xi_{-\mathbf{k}}^* \rangle = K_{w\mathbf{k}} - K_{v\mathbf{k}} + i\text{Re}\langle u_{v\mathbf{k}}^* u_{w\mathbf{k}} \rangle$. The terms in the right-hand side of Eq. (5) represent isotropic part, directional anisotropic part with respect to the direction of \mathbf{k} , and polarization anisotropic part with respect to the direction of \mathbf{u} of the kinetic energy [34]. In this work, the vertical kinetic energy

$$K_{z\mathbf{k}} = K_{\parallel\mathbf{k}} = \frac{K(k)}{8\pi k^2} \left(\frac{k_{\perp}}{k^2}\right)^2 + \frac{1}{2} \left(K_{\mathbf{k}} - \frac{K(k)}{4\pi k^2}\right) \left(\frac{k_{\perp}}{k^2}\right)^2 + \frac{1}{2} (K_{w\mathbf{k}} - K_{v\mathbf{k}}) \left(\frac{k_{\perp}}{k^2}\right)^2, \quad (6)$$

and its polarization anisotropic part, $K_{z\text{PA}\mathbf{k}}$, which is the last term in the right-hand side of Eq. (6), are used to quantify the anisotropy of a wave-number mode.

III. NUMERICAL RESULTS

A. Energy spectra

Spectra of total kinetic energy K , horizontal kinetic energy K_{\perp} , vertical kinetic energy K_{\parallel} , and potential energy V obtained in the numerical simulations with 2048³ grid points are shown in Fig. 1. The one-dimensional total kinetic-energy spectrum as a function of the horizontal wave numbers, for example, is defined as

$$K(k_{\perp}) = \frac{1}{\Delta k_{\perp}} \sum'_{k'_{\perp}} \sum'_{k'_{\parallel}} \frac{1}{2} \langle |\mathbf{u}_{k'_{\perp}, k'_{\parallel}}|^2 \rangle, \quad (7)$$

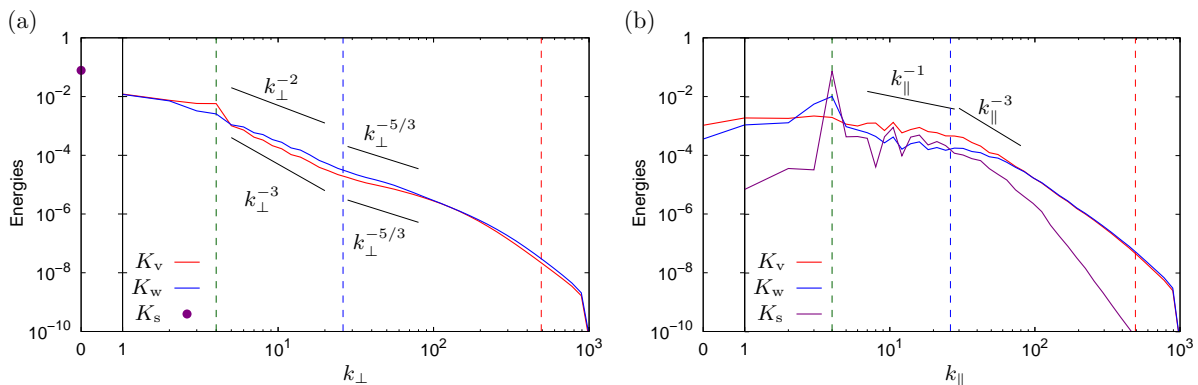


FIG. 2. (a) Horizontal wave-number spectra and (b) vertical wave-number spectra of vortical kinetic energy, wave kinetic energy and shear energy. The abscissa is scaled linearly for $k_{\perp}, k_{\parallel} \leq 1$ and logarithmically for $k_{\perp}, k_{\parallel} \geq 1$. See also the caption of Fig. 1 for the vertical lines.

where the summation $\sum'_{k'_{\perp}}$ is taken over $||\mathbf{k}'_{\perp}| - k_{\perp}| < \Delta k_{\perp}/2$, and Δk_{\perp} is the bin width to obtain the spectrum. The summation $\sum_{k'_{\parallel}}$ is taken over all the vertical wave number. These one-dimensional spectra are referred to as integrated spectra in this paper. Figure 1(a) shows the energy spectra as functions of the horizontal wave numbers integrated over the vertical wave numbers, while Fig. 1(b) shows those as functions of the vertical wave numbers integrated over the horizontal wave numbers. Note that although the forced wave number k_f is marked for reference in the figures, the forced wave numbers exist in the range $k_{\perp} < k_f$ and $k_{\parallel} < k_f$ because $|\mathbf{k}| = (k_{\perp}^2 + k_{\parallel}^2)^{1/2}$. The buoyancy wave number k_b and the Ozmidov wave number k_O have the same property. The integrated spectra show that the kinetic energy comes mostly from the horizontal component, and the potential energy spectra lies between the horizontal and vertical kinetic-energy spectra for all the wave numbers except for the horizontal wave-number spectra at the very large horizontal wave numbers.

The horizontal wave-number spectra have a relatively steep spectrum close to k_{\perp}^{-2} at the small horizontal wave numbers, and a less steep spectrum that is approximately $k_{\perp}^{-5/3}$ at the large horizontal wave numbers. The transition is observed approximately at the buoyancy wave number as reported in Ref. [21]. However, the energy spectrum at the large k_{\perp} in Fig. 1(a) is much steeper than that reported in Ref. [21], where the Kelvin-Helmholtz billows are supposed to generate the bump at the large horizontal wave numbers. It is worth pointing out that the computational box is flatter and that the hyper viscosity and the hyper diffusion are used in the simulation in Ref. [21]. Because of the flat computational box, the bump consists of the large vertical wave-number modes. The less steep energy spectra appear near the dissipation range in the inertial subrange, and they are due to the so-called bottleneck effect. The hyper viscosity and the hyper diffusion are known to enhance the bottleneck effect. One may observe that this horizontal wave-number spectrum is proportional to $k_{\perp}^{-5/3}$ in all the inertial subrange without any transition, but there actually exists a transition as seen below. Similar transition was observed in Refs. [4, 35]. Note that the range of the 3D Kolmogorov turbulence is too small to observe in the spectrum because the buoyancy Reynolds number is evaluated approximately as 2.1. The vertical wave-number spectra are also non-uniform, and the power laws at the small wave numbers and the large wave numbers are respectively close to those in Ref. [9] and Ref. [6]. Similarly to the horizontal wave-number spectra, the gradual transition is observed roughly at the buoyancy wave number. The steep spectra similar to k_{\parallel}^{-3} in the range $k_b < k_{\parallel} < k_O$ are due to balance between the inertia and the buoyancy [23, 36]. It is evident in these integrated spectra that the energy distribution is not scale-invariant and the energy spectra in the 2D domain spanned by the horizontal and vertical wave numbers show the anisotropy. It must be emphasized that these power laws of the integrated spectra consisting of the various slopes do not necessarily reflect the spectral structures unaffected by the boundary conditions. In this paper, the anisotropic energy distribution will be directly investigated below.

The coexistence of the different power-law exponents in the energy spectra, where the transition is observed approximately at the buoyancy wave number, is also observed in the horizontal wave-number spectra of the vortical kinetic energy and the wave kinetic energy (Fig. 2(a)). While the vortical energy spectrum and the wave kinetic energy spectrum are respectively close to k_{\perp}^{-3} and k_{\perp}^{-2} at the small horizontal wave numbers, both energy spectra approximately have $k_{\perp}^{-5/3}$ at the large horizontal wave numbers. The vertical wave-number spectra in Fig. 2(b) also exhibit the coexistence; the rather flat spectra appears at the small vertical wave numbers, and the steep spectra similar to the saturation spectrum k_{\parallel}^{-3} does at the large vertical wave numbers. These energy spectra are similar to

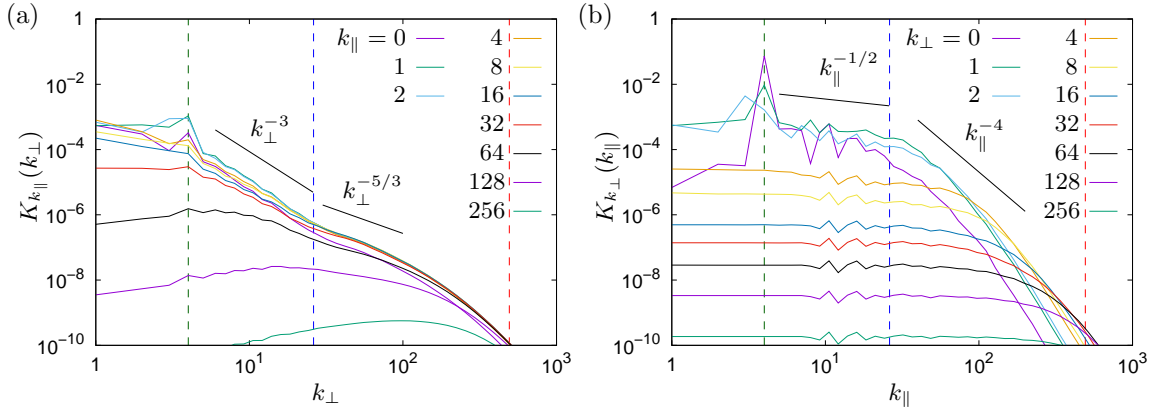


FIG. 3. Kinetic energy spectra (a) for each k_{\parallel} as function of k_{\perp} and (b) for each k_{\perp} as function of k_{\parallel} . See also the caption of Fig. 1 for the vertical lines.

the ones in Ref. [4]. The shear energy is defined only for $k_{\perp} = 0$, but it is large. In fact, the kinetic energies of the vortical, wave, and shear flows integrated over all the wave numbers are roughly 4×10^{-2} , 4×10^{-2} and 8×10^{-2} , respectively. The largest energy appears at $k_{\perp} = 0$ and $k_{\parallel} = 4$, which can be directly excited by the external force, as the shear energy. Note that although the external force excites both waves and vortices as well as the shear flows at a wave-number mode, and their amplitudes depend on the wave-number mode as recognized from the energies at the forced wave numbers in Fig. 2.

The non-uniformity of the horizontal wave-number spectra of the energies shown in Fig. 1(a) indicates the existence of the inner structure in the vertical wave-number spectra drawn in Fig. 1(b) and vice versa. The same applies to the vortical kinetic energy and the wave kinetic energy in Fig. 2. The horizontal wave-number spectra of the energies shown in Fig. 1(a) are obtained by integration over the vertical wave numbers, and the energy spectra without the integration are required to observe the inner structure. Such non-integrated kinetic-energy spectrum for each k_{\parallel} as a function of k_{\perp} is defined as

$$K_{k_{\parallel}}(k_{\perp}) = \frac{1}{\Delta k_{\perp}} \sum'_{k'_{\perp}} \frac{1}{\Delta k_{\parallel}} \sum'_{k'_{\parallel}} \frac{1}{2} \langle |\mathbf{u}_{k'_{\perp}, k'_{\parallel}}|^2 \rangle. \quad (8)$$

The non-integrated kinetic-energy spectrum for each k_{\perp} as a function of k_{\parallel} is similarly defined.

The non-integrated kinetic-energy spectra are drawn in Fig. 3. The kinetic-energy spectra as functions of k_{\perp} for $k_{\parallel} \leq 32$ shown in Fig. 3(a) are not so different from each other, since the vertical-energy spectra are the rather flat spectra as k_{\parallel}^{-1} as shown in Fig. 1(b). Nevertheless, we can observe that the energy spectra at small horizontal wave numbers become less steep roughly from k_{\perp}^{-3} to k_{\perp}^{-2} . As k_{\parallel} increases further, the maximal wave number moves to larger k_{\perp} . Most of the kinetic energy at small k_{\parallel} exists in $k_{\perp} \leq 2$ as shown in Fig. 3(b). The integrated energy spectra as functions of the vertical wave numbers shown in Fig. 1(b) consist of the corresponding non-integrated energy spectra in $k_{\perp} \leq 2$. It is consistent with the fact that the horizontal wave-number spectra uniformly and rapidly decrease as shown in Fig. 1(a). Moreover, in the range $30 \lesssim k_{\parallel} \lesssim 500$, the relatively flat spectrum close to $k_{\parallel}^{-1/2}$ extends to the large k_{\parallel} as k_{\perp} increases. Then, the large k_{\perp} has larger energy at the large k_{\parallel} than the small k_{\perp} has [36]. Thus, the integration over k_{\perp} makes the saturation spectrum complex in the large k_{\parallel} range. The saturation spectrum is considered to consist of the breaking of the internal gravity waves [37]. Since the integrated spectra of the kinetic energy shown in Figs. 1(a) and 1(b) are respectively obtained by summation of the non-integrated spectra shown in Figs. 3(a) and 3(b), the integrated spectra are determined mostly by the non-integrated spectra in the few small codimensional wave numbers. In this sense, the integrated spectra cannot properly reflect the energy distribution at the moderate wave numbers unaffected by the boundary conditions. Moreover, the identification of the dominant physical mechanism by the integrated spectra requires a careful inspection.

To observe the anisotropic structures of the energy spectra, the 2D spectra for total, vortical, wave kinetic, and potential energies in the horizontal and vertical wave-number domain are drawn in Fig. 4, which provides an overview of the energy spectra. The 2D spectrum is defined as

$$K(k_{\perp}, k_{\parallel}) = \frac{1}{2\pi k_{\perp}} \frac{1}{\Delta k_{\perp}} \sum'_{k'_{\perp}} \frac{1}{\Delta k_{\parallel}} \sum'_{k'_{\parallel}} \frac{1}{2} \langle |\mathbf{u}_{k'_{\perp}, k'_{\parallel}}|^2 \rangle, \quad (9)$$

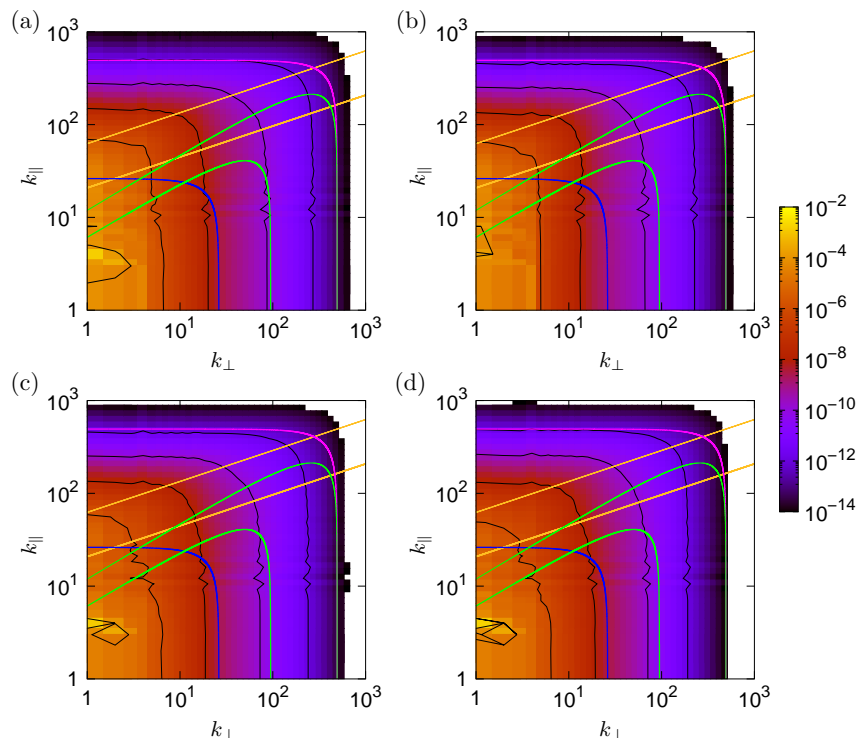


FIG. 4. 2D spectra of (a) total kinetic energy, (b) vortical energy, (c) wave kinetic energy, and (d) potential energy. The contours are drawn for $10^{-12}, 10^{-10}, \dots, 10^{-4}$. The critical wave number at which $\chi_{\mathbf{k}} = 1/3$ and that at which $\chi_{\mathbf{k}} = 1$ are represented by the thick and thin green curves, respectively. The 2D critical wave number at which $\chi_{2D\mathbf{k}} = 1/3$ and that at which $\chi_{2D\mathbf{k}} = 1$ are represented by the thick and thin yellow curves, respectively. The buoyancy wave number and Ozmidov wave number are respectively represented by the blue and magenta curves.

where the normalizing constant, $1/(2\pi k_{\perp})$, is introduced for the contours of the energy spectra to be compared easily with the completely isotropic ones.

All the energies shown in Fig. 4 accumulate at small k_{\perp} . It is consistent with the large energies at small k_{\perp} in the integrated and non-integrated spectra shown in Figs. 1–3. The energies drawn as the 2D spectra obviously show the anisotropy in small k_{\perp} and k_{\parallel} . As $k = \sqrt{k_{\perp}^2 + k_{\parallel}^2}$ becomes large, the contours of each energy are more similar to the isotropic curves which show the buoyancy wave number and the Ozmidov wave number. Such fact indicates that the anisotropy that exists at the small k gradually decreases and the flow at these scales is closer to the 3D isotropic Kolmogorov turbulence, as k become large. Note that even at the Ozmidov wave number the energy in $k_{\perp} < k_{\parallel}$ is larger than that in $k_{\perp} > k_{\parallel}$, and the energy spectra are still weakly anisotropic.

It is not clear in Fig. 4 where the wave kinetic energy and the potential energy are larger than the vortical energy. Furthermore, the four 2D energy spectra may appear close enough. However, by careful observation, we can find that the spectra of the wave kinetic energy (Fig. 4(c)) and the potential energy (Fig. 4(d)) are similar, but the vortical-energy spectrum (Fig. 4(b)) is different from these.

B. Distribution of turbulence indices in wave-number space

It is indispensable to separate the wave-number space based on the dominant physical mechanisms of turbulence. In particular, the theory of the critical balance needs the separation of the wave-dominant range. To quantitatively discuss whether the balance between linear and nonlinear time scales can identify the wave-dominant range, the energy decomposition written in Sec. II C is employed for the definition.

The difference of the vortical energy from the wave kinetic energy and the potential energy, and the similarity of the wave kinetic energy and the potential energy can be used to characterize the wave turbulence and the strong turbulence. In the wave-dominant range, the wave kinetic energy is postulated to be much larger than the vortical energy. The weak nonlinearity assumes that the wave kinetic energy is also expected to be close to the potential

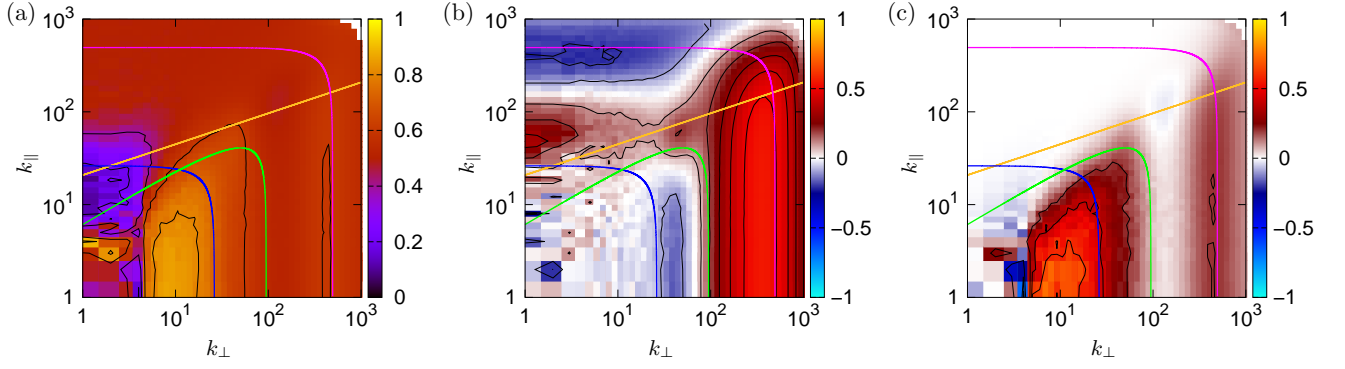


FIG. 5. (a) ratio of the wave kinetic energy to the total kinetic energy K_{wk}/K_k , (b) relative difference between the wave kinetic energy and the potential energy $(K_{wk} - V_k)/(K_{wk} + V_k)$, and (c) ratio of the polarization anisotropic part to the kinetic energy K_{zPAk}/K_k . The contours are drawn for every 0.2 in (a) and (c), and for every 0.1 in (b). The critical wave number at which $\chi_k = 1/3$, the 2D critical wave number at which $\chi_{2Dk} = 1/3$, the buoyancy wave number, and the Ozmidov wave number are represented by the green, yellow, blue, and magenta curves, respectively.

energy in the same range. Since the energies are not uniform in the wave-number space, a normalization of the energy is required to characterize each range; the ratios of the energies are drawn in Fig. 5 to quantify the dominance of the weak-wave turbulence. For example, the ratio of the wave kinetic energy to the total kinetic energy is used instead of direct comparison between the wave kinetic energy and the vortical energy.

The ratio of the wave kinetic energy to the total kinetic energy

$$\frac{K_{wk}}{K_k} = \frac{K_{wk}}{K_{vk} + K_{wk} + K_{sk}} \quad (10)$$

is drawn in Fig. 5(a). Note that the shear kinetic energy is defined only on $k_\perp = 0$, and it does not appear in Fig. 5(a). The weak turbulence theory requires that the linear time scale is much shorter than the nonlinear time scale, and the ratios of the nonlinear time scale to the linear time scale χ_k are usually $O(0.1)$. See Ref. [18] for example. It was reported in magnetohydrodynamic turbulence that the wave numbers at which the ratio of the nonlinear time scale to the linear time scale $\chi_k = 1/3$ are the critical wave numbers separating the weak and strong turbulence [27]. Note that the value $1/3$ is introduced as a rough indication because the transition between the wave-dominant range and the vortex-dominant range is gradual. In the present numerical simulation, the contour of $K_{wk}/K_k = 0.6$ is close to the curve of $\chi_k = 1/3$. The wave kinetic energy is dominant in the total kinetic energy over the vortical energy at the wave numbers where $\chi_k \gtrsim 1/3$. Note that the range of $k_\perp, k_\parallel < 5$ is directly affected by the external force, and is not considered here.

The dominance of the wave-kinetic energy does not always results in the weak-wave turbulence [38]. In the weak-wave turbulence, the wave-number modes must have the wave kinetic energy close to the potential energy. The relative difference between the wave kinetic energy and the potential energy

$$\frac{K_{wk} - V_k}{K_{wk} + V_k} \quad (11)$$

is drawn in Fig. 5(b). In the weak-wave turbulence, $K_w \approx V$, i.e., it is anticipated that the relative difference is close to 0 because of the weak nonlinearity. In fact, $-0.2 < (K_{wk} - V_k)/(K_{wk} + V_k) < 0.1$ in the range where $\chi_k \lesssim 1/3$. Therefore, the wave-number modes where the wave-kinetic energy is dominant over the vortical energy coincide with the modes which have the relative difference between the wave kinetic energy and the potential energy close to 0. Namely, the wave-number modes where $\chi_k \gtrsim 1/3$ is in the weak-wave turbulence.

Moreover, in Fig. 5(c), the ratio of the polarization anisotropic part to the total kinetic energy

$$\frac{K_{zPAk}}{K_k} = \frac{K_{wk} - K_{vk}}{2K_k} \left(\frac{k_\perp}{k} \right)^2 \quad (12)$$

is drawn. Here, $K_{zPAk} = \text{Re}[Z_k h_{+z\mathbf{k}}^2] = (k_\perp/k)^2 (K_{wk} - K_{vk})/2$ represents the polarization anisotropic part of the vertical kinetic energy according to the helical-mode decomposition. Equation (12) indicates the direct relation between the anisotropy and the dominance of the wave-kinetic energy over the vortical energy given by Eq. (10). In

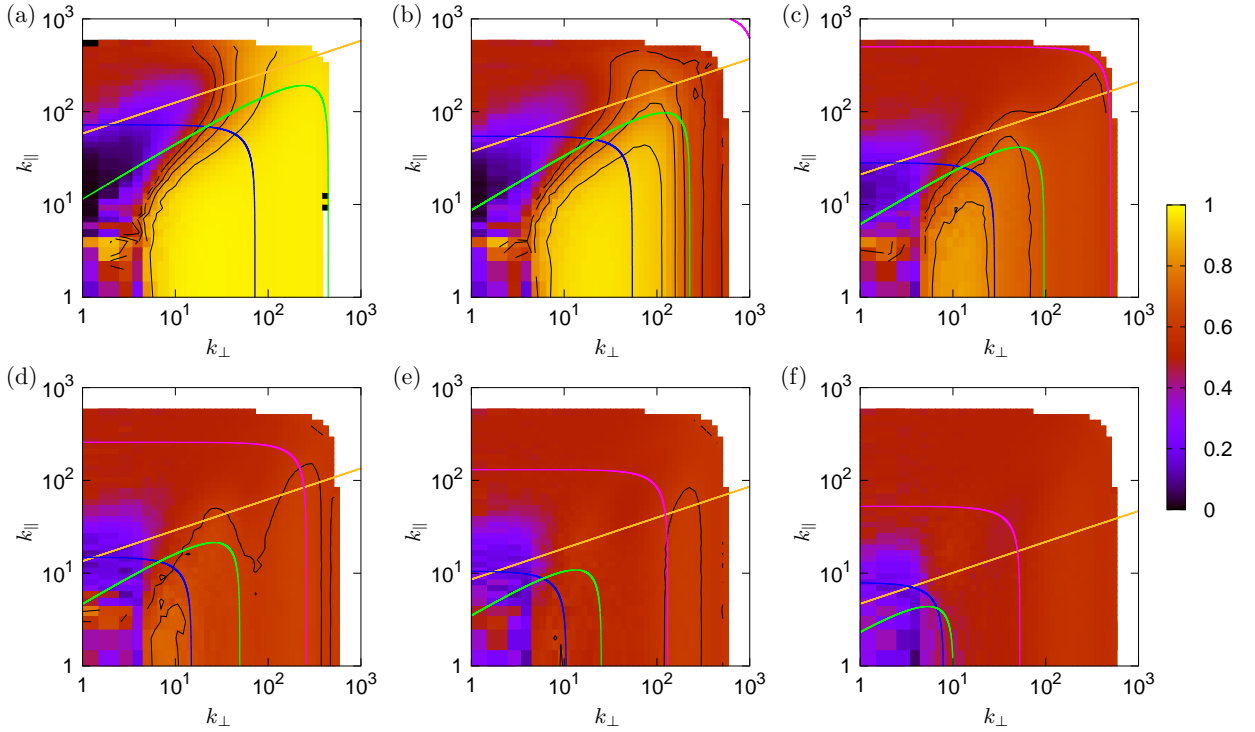


FIG. 6. Ratio of the wave kinetic energy to the total kinetic energy K_{wk}/K_k . (a) $\gamma_k = 0.1$, (b) 0.2, (c) 0.5, (d) 1, (e) 2, and (f) 5. See also the caption of Fig. 5 for the curves.

fact, the wave-number modes in the weak-wave turbulence, where $\chi_k \lesssim 1/3$, has $K_{zPAk}/K_k > 0.2$. The weak-wave turbulence of internal gravity waves has strong anisotropy.

The ratio of the gravity-wave period to the eddy-turnover time χ_k well separates the weak-wave turbulence also from the horizontally long waves $k_\perp \approx 1$ and $k_\parallel \sim O(10)$. The 2D ratio χ_{2Dk} also does it if $\chi_{2Dk} = 1/3$ is selected as a threshold, though χ_{2Dk} cannot separate the weak-wave turbulence from the 3D isotropic Kolmogorov turbulence by definition.

The wave-number range of the anisotropic weak-wave turbulence is smaller than the inner range of the Ozmidov wave number. The transient wave-number range from the anisotropic weak-wave turbulence to the 3D isotropic Kolmogorov turbulence appears in the middle of the two turbulence range, where the quasi-2D turbulence is dominant. In this transient range, the eddy-turnover time of the wave-number mode is larger than the Brunt-Väisälä period and is smaller than $1/3$ of the linear wave period of the mode. i.e., $1/N \lesssim \tau_k \lesssim 3/\sigma_k$, and the range is noticeable at the small horizontal and large vertical wave numbers. The wave-breaking is known to occur mainly at the small horizontal and large vertical wave numbers [39]. The saturation spectrum $K(k_\parallel) \propto k_\parallel^{-3}$ is observed in this range as shown in Fig. 1(b).

In the wave-number range $k_\perp \gg k_\parallel$, $K_w = (k/k_\perp)^2 K_\parallel \approx K_\parallel$, and $K_v \approx K_\perp$. Therefore, the horizontal energy spectrum $K_\perp \propto k_\perp^{-5/3}$ shown in Fig. 1(a) results mainly from the vortical mode. The fact that $K_w > K_v$ indicates that $K_\parallel > K_\perp$ in the wave-number range, which is confirmed by drawing K_\parallel/K though the figure is omitted. The weak-wave turbulence is stronger than the quasi-2D turbulence in the range where $\chi_k \lesssim 1/3$. In addition, the quasi-2D turbulence, i.e., the pancake turbulence [23] is dominant in the small k_\perp and large k_\parallel range where $\chi_k \gtrsim 1/3$ and $k < k_O$.

The wave period given by the linear dispersion relation characterizes the weak-wave turbulence better than the the Brunt-Väisälä period as seen in Fig. 5. To confirm it, the ratios of the wave kinetic energy to the total kinetic energy for different amplitudes of the external force are drawn in Fig. 6. The numerical simulations to draw Fig. 6 are performed by using 1024^3 grid points. The amplitude of the external force γ_k is varied from 0.1 to 5 in the low-resolution simulations for comparison with $\gamma_k = 0.5$, which is used to draw Figs. 1–5.

The range of the weak-wave turbulence is the largest when the external force is the smallest (Fig. 6(a)), and the range becomes smaller as the external force is larger. (Figs. 6(b)–6(e)) It results from the fact that the eddy-turnover time becomes smaller as the turbulent fluctuation is more excited. The threshold $\chi_k = 1/3$ well separates the weak-wave

turbulence independently of the buoyancy Reynolds number and the vertical Froude numbers considered here. For $\gamma_{\mathbf{k}} = 1$, the wave-number range of $\chi_{\mathbf{k}} \lesssim 1/3$ and hence the number of the wave-number modes are small. (Fig. 6(f)) Then, the weak-wave turbulence cannot be organized because the resonant interactions are rare. Such divergence in the simulation with this large external force is consistent with the break in the monotonicity of the Reynolds number and the vertical Froude number in Table I. It is derived from the limitation of numerical simulations due to the discretization and the periodic boundary condition. The wave-dominant range should exist even for this buoyancy Reynolds number and the Froude number, if the simulations in a much larger computational domain, which provides denser grid points in the wave-number space, were performed.

C. Deviation from linear dispersion relation in wave-number space

It has been exhibited in the previous subsection that the ratios of the nonlinear time scale to the linear time scale $\chi_{\mathbf{k}}$ i.e., the characteristic times can successfully separate the wave-dominant range by using the Cartesian decomposition and the helical-mode decomposition. To observe that the dominance of the waves in the range where $\chi_{\mathbf{k}} \lesssim 1/3$ in another way, a frequency deviation from the linear dispersion relation is evaluated. It is convenient to introduce a complex amplitude used in the weak turbulence theory [40]. The complex amplitude in the present system is defined as

$$a_{\mathbf{k}} = \frac{1}{\sqrt{2\sigma_{\mathbf{k}}}} \left(u_{z\mathbf{k}} - \frac{i}{N} b_{\mathbf{k}} \right). \quad (13)$$

Because the linear inviscid non-diffusive equation (4) can be rewritten as $\partial a_{\mathbf{k}}/\partial t = -i\sigma_{\mathbf{k}}a_{\mathbf{k}}$, the frequency spectrum of $a_{\mathbf{k}}$ has a value only at $-\sigma_{\mathbf{k}} = -Nk_{\perp}/k$ in the linear inviscid non-diffusive limit. The minus sign in front of the frequency comes from the conventional expression of the canonical equation in the weak turbulence theory. A frequency deviation is defined as

$$\delta\sigma_{\mathbf{k}} = \left(\frac{\sum_{\sigma} (\sigma + \sigma_{\mathbf{k}})^2 |\tilde{a}_{\mathbf{k},\sigma}|^2}{\sum_{\sigma} |\tilde{a}_{\mathbf{k},\sigma}|^2} \right)^{\frac{1}{2}}, \quad (14)$$

where $\tilde{a}_{\mathbf{k},\sigma}$ denotes the Fourier coefficient obtained from the time series of $a_{\mathbf{k}}(t)$. The relative frequency deviation, $\delta\sigma_{\mathbf{k}}/\sigma_{\mathbf{k}}$, is employed for the measure of the wave nature of a wave-number mode in this paper. When the weakly nonlinear wave mode is dominant at a wave-number mode, the frequency spectrum is narrow-band and it has a peak at the frequency given by the linear dispersion relation, and the relative frequency deviation of the wave-number mode is small. Conversely, when the nonlinearity is not weak owing to the vortical mode and/or other wave-number modes, the frequency spectrum is broad-band or it has peaks away from the linear frequency [38], and the relative frequency deviation is large. Note that the nonlinearity changes the frequency spectrum in two ways: one is the excitation of frequencies which do not satisfy the dispersion relation due to the nonlinear interactions among wave-number modes, and the other is the frequency shift due to the small-wave-number flows such as the Doppler effect.

The relative frequency deviation is drawn in Fig. 7. The frequency spectra are obtained from the time series of $a_{\mathbf{k}}$, where $\mathbf{k} = (k_x, k_y, k_z) = (0, 2^p, 2^q)$ and $p, q = 0, 1, 2, \dots$, in the high-resolution simulation. The relative frequency deviation is small in the range where $\chi_{\mathbf{k}} \lesssim 1/3$, and shows similarity to χ , becoming large as χ increases. This results from the increase of the band width of the frequency spectrum due to the nonlinearity. One may notice that the difference between the contours of the relative frequency deviation and χ at the large horizontal wave numbers where $k_y = 32, 64$ and $k_z \leq 16$ is relatively large. The difference can be interpreted by the Doppler shift due to the horizontal flows with the small horizontal wave numbers including the vertically-sheared horizontal flows having most of the total energy in the flow field as recognized from Figs. 1–3. Then, the dominance of the weakly nonlinear wave mode in the range where $\chi_{\mathbf{k}} \lesssim 1/3$ is supported by the frequency deviation of wave-number modes.

IV. CONCLUDING REMARK

In this paper, direct numerical simulations of strongly stratified turbulence where the internal gravity-wave turbulence and the strong turbulence coexist were performed. The energies accumulate at the small horizontal wave numbers, and the energies at the small vertical wave numbers are also large. Then, the one-dimensional spectra, which are obtained by the integration over the horizontal or vertical wave numbers, or by using the norm of the wave-number vector, mask the inner structures, and do not appropriately represent the critical wave numbers separating the

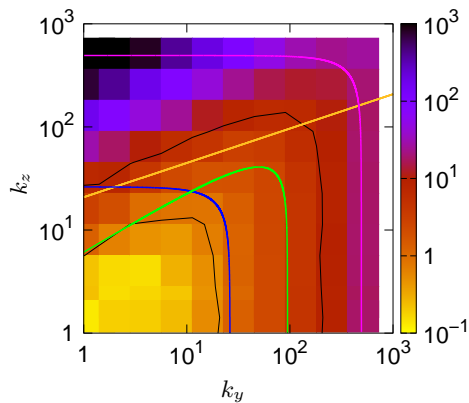


FIG. 7. Relative frequency deviation $\delta\sigma_{\mathbf{k}}/\sigma_{\mathbf{k}}$ for $\mathbf{k} = (k_x, k_y, k_z) = (0, 2^p, 2^q)$ where $p, q = 0, 1, 2, \dots$. The contours are drawn for 1 and 10. See also the caption of Fig. 5 for the curves.

wave-number range of the weak-wave turbulence. The non-integrated spectra and the two-dimensional spectra drawn in the horizontal and vertical wave-number domain reveal the inner structures of the anisotropic turbulence. The results show that the power laws observed in the one-dimensional spectra are superposition of various distributions of the spectral amplitude. Therefore, much care should be taken when the spectra are compared with the experimentally observed spectra, which are mostly obtained from one-dimensional time series.

Following the premise that the wave kinetic energy is much larger than the vortical energy, and is close to the potential energy in the range of the weak-wave turbulence, non-dimensional indices based on the energies, Eqs. (10)–(11), were proposed to determine the range in the wave-number space. It was also clarified by another non-dimensional index based on the energies, Eq. (12), that the polarization anisotropy in the range is large, resulting from the wave kinetic energy being larger than the vortical energy. These non-dimensional indices proposed in this paper show the similar distribution, which confirms the appropriateness of the indices for the identification of the range of the anisotropic weak-wave turbulence. The dominance of the waves in the range is also verified by the frequency spectra having peaks at the frequency given by the linear dispersion relation.

From the distributions of the non-dimensional indices in the horizontal and vertical wave-number domain, it was found that the range, which emerges at the small horizontal and vertical wave numbers, is anisotropic and smaller than the inner range of the Ozmidov wave number. The wave-number modes in the weak-wave turbulence have the linear time scale given by the linear dispersion relation smaller than $1/3$ of the nonlinear time scale, which is the eddy-turnover time. In other words, the critical wave number which separates the weak-wave turbulence has the ratio of the linear time scale to the nonlinear one being $1/3$. In most anisotropic turbulence systems, we have some options for linear and nonlinear time scales. The present results show that the range of the anisotropic weak-wave turbulence in the wave-number space can be identified when the appropriate time scales are selected in consideration of the anisotropy of the flow field.

The difference between the linear period given by the linear dispersion relation and the isotropic Brunt-Väisälä period is large in the range where the horizontal wave numbers are small and the vertical wave numbers are relatively large. The dynamics in the wave-number range is determined neither by the weak-wave turbulence nor by the three-dimensional isotropic Kolmogorov turbulence. The wave breaking is dominant in this wave-number range [41], and it is consistent with the saturation spectrum in Fig. 1(b). The critical balance states the energy transfer from the waves to the eddies in this range. In this sense, the coexistence of the waves and eddies might play an important role in the energy spectrum [33, 42]. The critical balance is the energy transfer in such transitional wave-number range between the wave-dominant and vortex-dominant ranges. The separation of the weak-wave turbulence in the present paper suggests that the critical balance should appear in the wave-number range $1/N \lesssim \tau_{\mathbf{k}} \lesssim 3/\sigma_{\mathbf{k}}$. The energy transfer in the transitional wave-number range will be reported elsewhere.

ACKNOWLEDGMENTS

Numerical computation in this work was carried out at the Yukawa Institute Computer Facility, Kyoto University and Research Institute for Information Technology, Kyushu University. This work was partially supported by JSPS

KAKENHI Grant No. 15K17971, No. 16K05490, No. 17H02860, and No. 18K03927.

-
- [1] W. H. Munk, Abyssal recipes, *Deep-Sea Res.* **13**, 707 (1966).
- [2] T. L. Clark, W. D. Hall, R. M. Kerr, D. Middleton, L. Radke, F. M. Ralph, P. J. Neiman, and D. Levinson, Origins of aircraft-damaging clear-air turbulence during the 9 December 1992 Colorado downslope windstorm: Numerical simulations and comparison with observations, *J. Atmos. Sci.* **57**, 1105 (2000).
- [3] G. D. Nastrom, K. S. Gage, and W. H. Jasperson, Kinetic energy spectrum of large-and mesoscale atmospheric processes, *Nature* **310**, 36 (1984).
- [4] Y. Kimura and J. R. Herring, Energy spectra of stably stratified turbulence, *J. Fluid Mech.* **698**, 19 (2012).
- [5] E. Lindborg, The energy cascade in a strongly stratified fluid, *J. Fluid Mech.* **550**, 207 (2006).
- [6] S. A. Smith, D. C. Fritts, and T. E. Vanzandt, Evidence for a saturated spectrum of atmospheric gravity waves, *J. Atmos. Sci.* **44**, 1404 (1987).
- [7] R. Bolgiano, Turbulent spectra in a stably stratified atmosphere, *J. Geophys. Res.* **64**, 2226 (1959).
- [8] A. M. Obukhov., On influence of buoyancy forces on the structure of temperature field in a turbulent flow, *Dokl Acad Nauk SSSR* **125**, 1246 (1959).
- [9] C. J. R. Garrett and W. H. Munk, Internal waves in the ocean, *Annu. Rev. Fluid Mech.* **11**, 339 (1979).
- [10] Y. Lvov, E. Tabak, K. Polzin, and N. Yokoyama, Oceanic internal wavefield: Theory of scale invariant spectra, *J. Phys. Oceanogr.* **40**, 2605 (2010).
- [11] C. S. Gardner, C. A. Hostetler, and S. J. Franke, Gravity wave models for the horizontal wave number spectra of atmospheric velocity and density fluctuations, *J. Geophys. Res.-Atmos.* **98**, 1035 (1993).
- [12] J. K. Kevorkian and J. D. Cole, *Multiple Scale and Singular Perturbation Methods*, Applied Mathematical Sciences, Vol. 114 (Springer-Verlag New York, 1996).
- [13] L. Biven, S. V. Nazarenko, and A. C. Newell, Breakdown of wave turbulence and the onset of intermittency, *Phys. Lett. A* **280**, 28 (2001).
- [14] A. C. Newell, S. Nazarenko, and L. Biven, Wave turbulence and intermittency, *Physica D* **152–153**, 520 (2001).
- [15] L. J. Biven, C. Connaughton, and A. C. Newell, Structure functions and breakdown criteria for wave turbulence, *Physica D* **184**, 98 (2003).
- [16] N. Yokoyama and M. Takaoka, Hysteretic transitions between quasi-two-dimensional flow and three-dimensional flow in forced rotating turbulence, *Phys. Rev. Fluids* **2**, 092602 (2017).
- [17] R. Meyrand, K. H. Kiyani, O. D. Gürçan, and S. Galtier, Coexistence of weak and strong wave turbulence in incompressible hall magnetohydrodynamics, *Phys. Rev. X* **8**, 031066 (2018).
- [18] N. Yokoyama and M. Takaoka, Identification of a separation wave number between weak and strong turbulence spectra for a vibrating plate, *Phys. Rev. E* **89**, 012909 (2014).
- [19] W. F. Vinen and J. J. Niemela, Quantum turbulence, *J. Low Temp. Phys.* **128**, 167 (2002).
- [20] R. V. Ozmidov, On the turbulent exchange in a stable stratified ocean, *Izv. Acad. Sci., USSR, Atmos. Oceanic Phys.* **1**, 493 (1965).
- [21] M. L. Waite, Stratified turbulence at the buoyancy scale, *Phys. Fluids* **23**, 066602 (2011).
- [22] D. K. Lilly, Stratified turbulence and the mesoscale variability of the atmosphere, *J. Atmos. Sci.* **40**, 749 (1983).
- [23] P. Billant and J.-M. Chomaz, Self-similarity of strongly stratified inviscid flows, *Phys. Fluids* **13**, 1645 (2001).
- [24] S. V. Nazarenko and A. A. Schekochihin, Critical balance in magnetohydrodynamic, rotating and stratified turbulence: towards a universal scaling conjecture, *J. Fluid Mech.* **677**, 134 (2011).
- [25] P. Goldreich and S. Sridhar, Toward a theory of interstellar turbulence. II. strong Alfvénic turbulence, *Astrophys. J.* **438**, 763 (1995).
- [26] Y.-c. Ghim, A. A. Schekochihin, A. R. Field, I. G. Abel, M. Barnes, G. Colyer, S. C. Cowley, F. I. Parra, D. Dunai, and S. Zolotnik (the MAST Team), Experimental signatures of critically balanced turbulence in MAST, *Phys. Rev. Lett.* **110**, 145002 (2013).
- [27] R. Meyrand, S. Galtier, and K. H. Kiyani, Direct evidence of the transition from weak to strong magnetohydrodynamic turbulence, *Phys. Rev. Lett.* **116**, 105002 (2016).
- [28] P. Clark di Leoni, P. J. Cobelli, P. D. Mininni, P. Dmitruk, and W. H. Matthaeus, Quantification of the strength of inertial waves in a rotating turbulent flow, *Phys. Fluids* **26**, 035106 (2014).
- [29] A. Maffioli and P. A. Davidson, Dynamics of stratified turbulence decaying from a high buoyancy Reynolds number, *J. Fluid Mech.* **786**, 210 (2016).
- [30] L. M. Smith and F. Waleffe, Generation of slow large scales in forced rotating stratified turbulence, *J. Fluid Mech.* **451**, 145 (2002).
- [31] S. Nazarenko, *Wave Turbulence* (Springer, Heidelberg, 2011).
- [32] J. R. Herring, Approach of axisymmetric turbulence to isotropy, *Phys. Fluids* **17**, 859 (1974).
- [33] M. L. Waite and P. Bartello, Stratified turbulence generated by internal gravity waves, *J. Fluid Mech.* **546**, 313 (2006).
- [34] P. Sagaut and C. Cambon, *Homogeneous Turbulence Dynamics* (Cambridge University Press, 2008).
- [35] G. Brethouwer, P. Billant, E. Lindborg, and J.-M. Chomaz, Scaling analysis and simulation of strongly stratified turbulent flows, *J. Fluid Mech.* **585**, 343 (2007).

- [36] A. Maffioli, Vertical spectra of stratified turbulence at large horizontal scales, *Phys. Rev. Fluids* **2**, 104802 (2017).
- [37] E. M. Dewan and R. E. Good, Saturation and the “universal” spectrum for vertical profiles of horizontal scalar winds in the atmosphere, *J. Geophys. Res.* **91**, 2742 (1986).
- [38] H. A. Kafiabad and P. Bartello, Spontaneous imbalance in the non-hydrostatic Boussinesq equations, *J. Fluid Mech.* **847**, 614643 (2018).
- [39] C. H. McComas, Equilibrium mechanisms within the oceanic internal wave field, *J. Phys. Oceanogr.* **7**, 836 (1977).
- [40] V. E. Zakharov, V. S. L’vov, and G. Falkovich, *Kolmogorov Spectra of Turbulence I: Wave Turbulence* (Springer-Verlag, Berlin, 1992).
- [41] C. H. McComas and P. Müller, The dynamic balance of internal waves, *J. Phys. Oceanogr.* **11**, 970 (1981).
- [42] M. L. Waite and P. Bartello, Stratified turbulence dominated by vortical motion, *J. Fluid Mech.* **517**, 281 (2004).